Nanoscale

PAPER

View Article Online
View Journal | View Issue

Cite this: *Nanoscale*, 2020, **12**, 2820

Extracting the shape of nanometric field emitters

Daniel Beinke,[a] Felicitas Bürger,[b] Helena Solodenko,[a] Rachana Acharya,[c] Hagen Klauk[c] and Guido Schmitz *[a]

Received 24th September 2019,
Accepted 8th January 2020

DOI: 10.1039/c9nr08226c

rsc.li/nanoscale

The high resolution nanoanalysis by atom probe tomography is based on needle-shaped samples that represent nanometric field emitters with typical curvature radii of 50 nm. After field desorption and detection of a large set of atoms, the sample volume has to be numerically reconstructed. Conventionally, this reconstruction is performed with the assumption of a hemispherical apex. This established practice can lead to serious distortions of the tomography. In this work, we demonstrate how the real shape of the emitter can be extracted from the event density on the 2D detector setup. Except for convexity, no other restriction is imposed on the shape. The required mathematics is derived and the method is demonstrated with numerically simulated and experimental data sets of complex tip shapes. The computational effort of the method is also suitable to handle data sets of a few hundred million atoms.

Introduction

Atom probe tomography (APT) is a nanoscopic analysis method that delivers chemical information with single atom sensitivity and sub-nanometer spatial resolution. To this end, the atoms of needle-shaped samples with a few tens of nanometers apex radius are individually field-desorbed and detected by a 2D microchannel plate setup after a flight distance of about 10 cm. The time-of-flight (ToF), as well as the impact position are recorded.[1–3] While identification of the desorbed species by ToF spectroscopy is still a straight-forward task, the spatial reconstruction of the desorbed volume from the detected events is more delicate. In principle, the trajectories of the desorbed species must be accurately known to derive the original positions on the emitter surface.[4]

After a short running-in period, homogeneous samples develop a universal shape that is usually expected as an almost hemispherical apex of which only the isotropic curvature radius may further increase during the measurement. In this case, a normalized field distribution and thus a normalized shape of the trajectories can be assumed. This allows a determination of the original atom positions by a simple point projection[5] of which the center is located between that of a stereographic and a gnomonic projection, rather than calculating the explicit trajectories. However, it is well-known that in the case of field emitters with a heterogeneous phase structure and thus heterogeneous evaporation behaviour, the emitter shape can severely deviate from this universal geometry.[6–9] Owing to a lack of knowledge, the hemispherical apex is nevertheless assumed, which may lead to significant distortions in the reconstruction. These are known as local magnification artefacts to the APT community and may become so severe that they fully mislead the interpretation.[10–13]

Despite the remarkable technical improvements of APT instrumentation, the reconstruction protocols have not changed fundamentally over the last twenty years. The point projection approach scaled by the momentary radius of the tip, as introduced by Bas *et al.*[5] still forms the basis of all practical work except for minor modifications in projection angles and volume increment to better grasp the large angle aperture of modern instruments. A few attempts to improve the reconstruction while pertaining a hemispherical emitter have been made in the past.[14–17] Concepts to relax the spherical symmetry are rare. De Geuser *et al.*[18] demonstrated a post-treatment of the reconstructions that takes into account heterogeneous evaporation parameters after the principle microstructure has been identified in a first rough reconstruction step. More recently, an analytical description of the emitter curvature has been suggested under the assumption of fixed mean curvatures for the particular geometry of a bilayer[19] and even multilayers.[20] This allows the development of a reconstruction protocol for atom probe tips of axial symmetry that contain stacked multilayer structures.[21] Beinke *et al.*[4] introduced the concept of reversing the reconstruction order, which enables a numerical calculation of realistic trajectories for an arbitrary emitter shape. However, the inaccuracy introduced by the finite detector efficiency and the extended numerical effort have hindered the development of a code for practical analysis yet.

[a]*Chair of Materials Physics, Institute for Materials Science, University of Stuttgart, Heisenbergstr. 3, D-70569 Stuttgart, Germany.*
E-mail: guido.schmitz@imw.uni-stuttgart.de
[b]*Fakultät für Mathematik, Universität Regensburg, D-93040 Regensburg, Germany*
[c]*Max Planck Institute for Solid State Research, Heisenbergstr. 1, D-70569 Stuttgart, Germany*

Presently, several initiatives are known for constructing combined instruments that allow correlative electron microscopy *in situ* during the field desorption and thus to determine the shape of the field emitter. This requires rather large investments and the development of complex instrumentation. In this communication, we follow a fundamentally different concept. Instead of performing additional microscopy, we show how to derive the unknown shape of the field emitter from the statistical distribution of the detected events, making use of more substantial mathematics. To this end, a subset of the data is selected, on the one hand, small enough that the tip shape stays practically constant during evaporation of the respective species, but on the other hand, large enough to evaluate the event distribution on the detector with sufficient statistical significance. In a recent conference report,[22] Beinke *et al.* introduced the fundamental idea of a statistical shape extraction and showed how it could be used to design a complete reconstruction protocol. At that time, however, the proposed procedure was still restricted to samples that obey cylindrical symmetry, since a mathematical solution for arbitrary shapes had not been found. Now, we are in the position to relieve this restriction and present a general solution for asymmetrically shaped field emitters. As the only remaining requirement, we still impose the convexity of the volume, which is a very reasonable presumption for the typical situation of steady-state field evaporation of pore-free materials. In general, samples with a partly concave surface bear the risk of trajectory overlap and, therefore, the risk of an artificial chemical mixing. They should be avoided in practical analysis.

Fundamental equations of the curved emitter surface in 3D space

In the following, we will describe the emitter surface as a height profile in cylindrical coordinates:

$$\mathbf{h} = \begin{pmatrix} r\cos\varphi \\ r\sin\varphi \\ h(r,\varphi) \end{pmatrix}. \tag{1}$$

Provided a free choice of the function $h = h(r, \varphi)$, any convex shape of the apex can be described in this way. For later analysis, we also need to require that the shape must be smooth, *i.e.* the height function must be sufficiently differentiable. The definition of the variables is illustrated in Fig. 1. The shown measurement geometry consists of the needle-shaped sample (field emitter) that points towards the two-dimensional detector plane. Aside from the cylindrical coordinates r, φ, h, we define the distance D between the ion impact position and the detector center, as well as the azimuthal detection angle Φ_D of the detected event. Neglecting effects of atomic roughness at the surface, the ions launch perpendicular from the mesoscopic emitter surface. Owing to the electrostatic effect of the sample shaft, the field lines and, to a lesser extent, the ion trajectories also bend toward the detector axis. Thus, strictly the

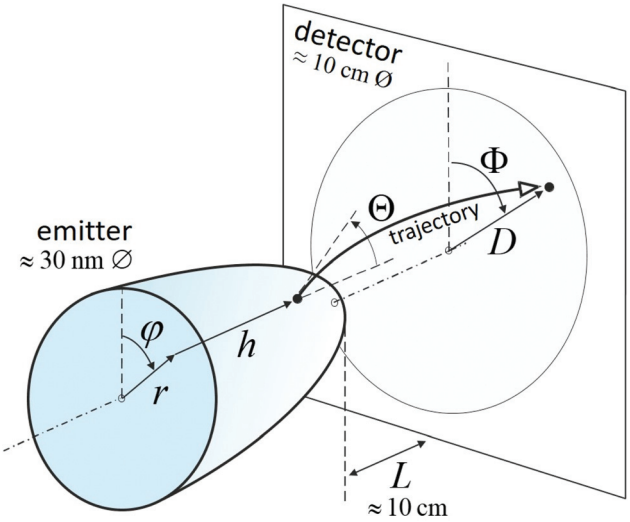

Fig. 1 Measurement geometry of atom probe tomography with the definition of important geometric parameters. Note that the sketch is not drawn to realistic scale. In reality, the emitter is much smaller than the detector width or the spacing L between tip and detector.

polar detection angle, defined as $\tan\Theta_D := D/L$, is usually smaller than the polar launching angle Θ. However, as an experimental matter of fact, the polar launching angle relates to very good approximation linearly to the radial distance D on the detector plane[23]

$$\Theta = \kappa \cdot D/L, \tag{2}$$

if the angle is restricted to the finite aperture of present-day instruments (about 45°). The hereby introduced imaging compression factor κ and the flight distance L are instrumental constants. As a consequence, by suitable scaling of the detector coordinates, the radial distance D on the detector plane can be directly identified with the polar launching angle Θ from the emitter surface. On the same level of approximation, the azimuthal launching and the detection angle are assumed being identical ($\Phi_D = \Phi$).

To determine the local surface normal which represents the launching direction, we first calculate two linearly independent tangential vectors:

$$\partial_r\mathbf{h} = \begin{pmatrix} \cos\varphi \\ \sin\varphi \\ h_r \end{pmatrix}; \quad \partial_\varphi\mathbf{h} = \begin{pmatrix} -r\sin\varphi \\ r\cos\varphi \\ h_\varphi \end{pmatrix} \tag{3}$$

(here and in the following a sub-index r or φ denotes the respective partial derivative) and construct the perpendicular direction as the vector product:

$$\begin{aligned} &\mathbf{n} := \partial_r\mathbf{h} \times \partial_\varphi\mathbf{h} \\ &\begin{pmatrix} n_x \\ n_y \\ n_z \end{pmatrix} = \begin{pmatrix} h_\varphi\sin\varphi - r\cdot h_r\cos\varphi \\ -h_\varphi\cos\varphi - r\cdot h_r\sin\varphi \\ r \end{pmatrix}. \end{aligned} \tag{4}$$

This surface normal defines the initial direction of the ions. It translates into the polar and azimuthal launching (= detection) angles *via* the following equations:

$$\tan\Theta := \frac{\sqrt{{n_x}^2 + {n_y}^2}}{n_z} = \frac{\sqrt{{h_\varphi}^2 + r^2{h_r}^2}}{r} \quad (5)$$

$$\tan\Phi := \frac{n_y}{n_x} = \frac{r \cdot h_r \sin\varphi + h_\varphi \cos\varphi}{r \cdot h_r \cos\varphi - h_\varphi \sin\varphi}. \quad (6)$$

By combining eqn (5) and (6) and through the application of substantial algebra, we eventually find two convenient expressions for the partial derivatives of the local height profile:

$$h_r = -\tan\Theta \cdot \cos(\Phi - \varphi), \quad (7)$$

$$h_\varphi = -r \tan\Theta \cdot \sin(\Phi - \varphi). \quad (8)$$

In axial symmetric structures $h_\varphi \equiv 0$ holds. Thus, for this case, the azimuthal detection angle Φ can be identified with the sample coordinate azimuth φ. But this identity is not valid in general. In the following considerations, we have to distinguish the sample azimuth φ strictly from the detection azimuth Φ.

The fundamental concept of the shape extraction

The principle of the shape extraction from a sufficiently large set of detected events shall first be illustrated with a quasi 2D situation of axial symmetry illustrated in Fig. 2. During field evaporation, the emitter necessarily shrinks due to continuous desorption of atoms. However, for a steady-state situation in which the spatial distribution of the different phases at the surface remains almost constant, the surface only changes in a self-similar manner, *i.e.* besides a rigid shift towards the emitter base, the height profile may only scale by a unique factor, usually the average tip radius, that captures the blunting of the tip. In Fig. 2a, we have even neglected this blunting, since it subsequently does not affect the relative densities of events on the detector plane. Obviously, the number of atoms evaporated into a given angular direction (Θ, $\Theta + \Delta\Theta$) must correspond to the volume (grey shaded) between the two consecutive profiles. Furthermore, as indicated at the bottom of the figure, this volume is most easily calculated by projecting the surface to the emitter base. Consequently, the volume corresponds to the projected area a_p times the rigid shift $|\Delta z|$ between the two height profiles. Technically, we may discretize the height profile into segments with constant increment $\Delta\Theta$ in between (see Fig. 2b). Atoms evaporated from a given surface segment must hit the detector at a predefined angular range. Each of them represent a tiny volume portion. For the sake of simplicity, we can assume that all events have the same (atomic) volume portion V_{at}. A generalization to species of varying size can nevertheless be achieved since each event is identified by time-of-flight mass spectrometry.

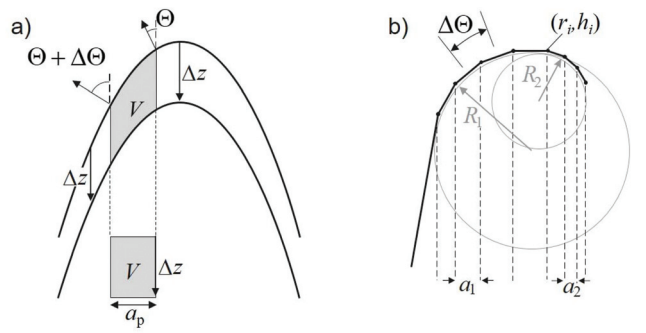

Fig. 2 Principle of steady-state evaporation. (a) In the case of a cylindrical shaft, a rigid surface is shifted downwards (sample shrinks). The evaporated volume is given by the projection to the base times the shifted length ($a_p \times \Delta z$). (b) The local curvature is related to the number of atoms measured in a given direction of the detector. A higher number of detected atoms per angular range correlates with a larger surface or base segment (a_1 instead of a_2) per angular range and thus a larger radius (R_1 instead of R_2).

As the shift between the height profiles is constant along the surface, a relatively higher density of events in a particular detector direction must correspond to a relatively larger projected size of the respective segment. Fig. 2b demonstrates how this interpretation of the data ultimately yields a varying local curvature of the surface. A group of larger segments leads to less curvature (larger radius R_1), a group of shorter segments to higher curvature (smaller radius R_2). In a previously presented evaluation protocol,[22] we hold the inclinations of the surface segments constant, but vary the discrete vertices (r_i,h_i) to adjust the segment sizes a_i to the measured local density of detected events.

It should be noted here, that the proposed data interpretation only delivers relative size differences among the segments. Since the absolute scaling of the shift Δz is unknown, the size of the emitter cannot be obtained. Similar to the established scheme of Bas *et al.*,[5] we still need to determine the evolution of the average emitter radius by independent considerations, *e.g.* based on the evolution of the tip voltage, based on the assumption of constant shaft angle or by calibration of known lattice plan distances.

In a previous communication,[22] Beinke *et al.* have shown that a straight-forward application of the outlined concept leads to a feasible reconstruction protocol which improved the tomographic reconstruction significantly. However, this concept has still been restricted to sample geometries of axial symmetry and therefore of limited practical use. A generalization to arbitrary emitter shapes needs further considerations, as presented below.

The mathematical formulation for a non-axial symmetric surface shape

As a prerequisite for the next considerations, we assume that a continuous density function $\rho(\Theta, \Phi)$ on the detector plane has

been determined from the discrete data, so that the number of events measured in a defined region of the detector can be calculated as

$$N(\Theta,\Phi)\Delta\Theta\Delta\Phi = \int_{\Theta}^{\Theta+\Delta\Theta}\int_{\Phi}^{\Phi+\Delta\Phi}\rho(\Theta',\Phi')\cdot\Theta'\mathrm{d}\Theta'\mathrm{d}\Phi' \qquad (9)$$

(circular coordinates. Here, Θ represents the radial direction obtained after the proper scaling of the radial distance D into units of the polar angle Θ *via* eqn (2)). Assume, the principal radii of curvature be determined at a given point of the surface (for illustration see Fig. 3a). Since the corresponding two circles stand perpendicular to each other (or can be chosen so), $\mathrm{d}a = R_{\max}\mathrm{d}\beta{\cdot}R_{\min}\mathrm{d}\gamma$ represents a rectangular surface segment, given by the principal radii and arbitrarily small angle increments $\mathrm{d}\beta$ and $\mathrm{d}\gamma$. Atoms that launch perpendicularly from this segment, obviously travel along angular directions that are comprised in the solid angle $\mathrm{d}\Omega = \mathrm{d}\beta{\cdot}\mathrm{d}\gamma$. Provided a smooth convex shape of the surface, Ω and the surface a are linked by an unambiguous function. This allows calculating the differential,[24]

$$K := \frac{\mathrm{d}\Omega}{\mathrm{d}a} = \frac{1}{R_{\max}}\cdot\frac{1}{R_{\min}} \qquad (10)$$

also known as the Gaussian curvature, the inverse product of the two principal radii of curvature. In steady-state evaporation, we know (see previous section) that the number

$$\mathrm{d}N = \frac{\Delta z}{V_{\mathrm{at}}}\cdot\cos\Theta\,\mathrm{d}a \qquad (11)$$

of atoms need to evaporate from the surface segment $\mathrm{d}a$. These are detected in the solid angle $\mathrm{d}\Omega$. Rearranging eqn (11) for $\mathrm{d}a$ and inserting into eqn (10) leads to

$$K = \frac{\Delta z}{V_{\mathrm{at}}}\cdot\cos\Theta\cdot\frac{\mathrm{d}\Omega}{\mathrm{d}N} = \frac{\Delta z}{V_{\mathrm{at}}}\cdot\frac{\cos\Theta}{\rho}, \qquad (12)$$

representing the fundamental relation that allows interpreting the density ρ of detected events in terms of the curvature, which the correct sample surface must expose in a given angular direction.

If the surface is represented as a function graph in polar coordinates, differential geometry shows that[25]

$$K(\Theta,\Phi) = \frac{r^2 h_{r,r}(h_{\varphi,\varphi}+rh_r)-(h_\varphi - rh_{r,\varphi})^2}{\left[r^2(h_r{}^2+1)+h_\varphi{}^2\right]^2}, \qquad (13)$$

in which Θ and Φ are implicitly linked to r and φ through eqn (5) and (6). Thus, the numerical task is the determination of the height profile $h(r, \varphi)$ so that at each surface position, eqn (13) matches eqn (12) when evaluated at the corresponding angles $\Theta(r, \varphi)$ and $\Phi(r, \varphi)$ of the local surface normal.

Design of the computational algorithm

In the following, we describe the concrete algorithm to obtain a computational approximation of the emitter surface. The processing of a selected subset of events starts with the calculation of the event density. The detector, first scaled to the polar angle Θ (eqn (2)), is split into rings of constant polar angle increment $\Delta\Theta$. Each of these is further split into segments of the azimuthal increment $\Delta\Phi$. We calculate a discrete density from the numbers of atoms N_{Θ_i,Φ_j} counted on each detector segment

$$\rho_{\Theta_i,\Phi_j} := \frac{N_{\Theta_i,\Phi_j}}{\sin\Theta_i\cdot\Delta\Theta\Delta\Phi}. \qquad (14)$$

A continuous density function $\rho(\Theta, \Phi)$ needed in the later numerical integration is determined by bilinear interpolation between the concentric grid points.

The height profile has to be determined at the discrete positions $h_{i,j} = h(r_i, \varphi_j)$ (see Fig. 3b). In order to develop a finite

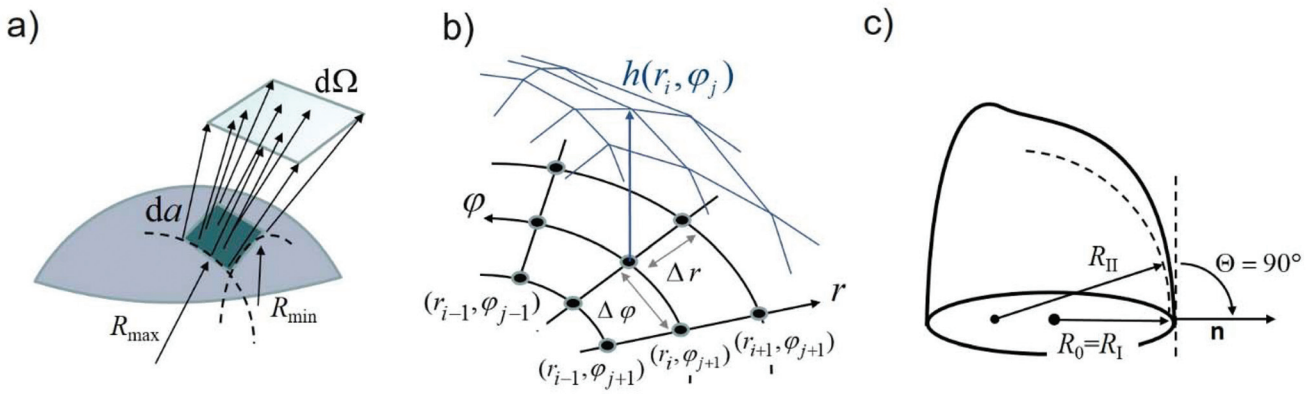

Fig. 3 Geometric details of the proposed algorithm: (a) fundamental relation between a selected part of the surface area and the orientation range within a solid angle. (b) Construction of the emitter surface $h(r_i, \varphi_j)$ on a discrete grid of base points (r_i, φ_j) regularly spaced by constant Δr and $\Delta\varphi$. To calculate $h(r_i, \varphi_j)$ in the finite difference iteration, the compact stencil of the eight direct neighbours of the point (r_i, φ_j) is used. (c) Boundary condition at the transition between the apex and the cylindrical shaft (at $\Theta = 90°$). One main curvature radius R_I approaches R_0, the second, R_{II}, follows from the respective Gaussian curvature.

differences scheme, by which eqn (13) can be solved iteratively, we approximate the required derivatives as

$$\frac{\partial h}{\partial r} \approx \frac{h_{i+1,j}^{(l)} - h_{i-1,j}^{(l)}}{2\Delta r}; \quad \frac{\partial h}{\partial \varphi} \approx \frac{h_{i,j+1}^{(l)} - h_{i,j-1}^{(l)}}{2\Delta \varphi}; \tag{15a, b}$$

$$\frac{\partial^2 h}{\partial r^2} \approx \frac{h_{i+1,j}^{(l)} + h_{i-1,j}^{(l)} - 2h_{i,j}^{(l+1)}}{\Delta r^2}; \quad \frac{\partial^2 h}{\partial \varphi^2} \approx \frac{h_{i,j+1}^{(l)} + h_{i,j-1}^{(l)} - 2h_{i,j}^{(l+1)}}{\Delta \varphi^2}; \tag{16a, b}$$

$$\frac{\partial^2 h}{\partial r \partial \varphi} \approx \frac{h_{i+1,j+1}^{(l)} + h_{i-1,j-1}^{(l)} - h_{i+1,j-1}^{(l)} - h_{i-1,j+1}^{(l)}}{\Delta r \Delta \varphi}. \tag{17}$$

Here, the index (l) indicates the iteration order. Noteworthy, the next iteration step $(l + 1)$ only appears in the unmixed second derivatives (eqn (16a,b)). Inserting eqn (15)–(17) into eqn (13) and solving for $h_{i,j}^{(l+1)}$, we obtain a quadratic equation that is solved as:

$$h_{i,j}^{(l+1)} = -\frac{\delta}{2} + \sqrt{\frac{\delta^2}{4} - \chi + \beta + \alpha \cdot K(\Theta_i, \Phi_j)}. \tag{18}$$

In the latter expression, we made use of the following convenient abbreviations:

$$\begin{aligned}
\alpha &:= \frac{\Delta r^2 \Delta \varphi^2}{4 r_i^2} \cdot \left[r_i^2 \left(1 + \left(\frac{h_{i+1,j}^{(l)} - h_{i-1,j}^{(l)}}{2\Delta r} \right)^2 \right) + \left(\frac{h_{i,j+1}^{(l)} - h_{i,j-1}^{(l)}}{2\Delta \varphi} \right)^2 \right]^2 \\
\beta &:= \frac{\Delta r^2}{4 r_i^2} \cdot \left[\frac{h_{i,j+1}^{(l)} - h_{i,j-1}^{(l)}}{2} - r_i \frac{h_{i+1,j+1}^{(l)} + h_{i-1,j-1}^{(l)} - h_{i+1,j-1}^{(l)} - h_{i-1,j+1}^{(l)}}{\Delta r} \right]^2 \\
\chi &:= \frac{1}{4} \left(h_{i+1,j}^{(l)} + h_{i-1,j}^{(l)} \right) \left(h_{i,j+1}^{(l)} + h_{i,j-1}^{(l)} \right) + \frac{\Delta \varphi^2}{8} \frac{r_i}{\Delta r} \left[\left(h_{i+1,j}^{(l)} \right)^2 - \left(h_{i-1,j}^{(l)} \right)^2 \right] \\
\delta &:= -\frac{1}{2} \left(h_{i+1,j}^{(l)} + h_{i-1,j}^{(l)} + h_{i,j+1}^{(l)} + h_{i,j-1}^{(l)} \right) - \frac{\Delta \varphi^2}{4} \frac{r_i}{\Delta r} \left(h_{i+1,j}^{(l)} - h_{i-1,j}^{(l)} \right)
\end{aligned} \tag{19a–d}$$

Expressions (19a–d) all depend exclusively on the height profile determined in the previous iteration step, so that the next $h_{i,j}^{(l+1)}$ can exactly be calculated by eqn (18).

In order to apply the iteration scheme within a finite region, suitable boundary conditions have to be set. These may either fix the height of the surface or the direction of its normal at the border of the calculation region. Any practical detection system is limited by a finite aperture that ignores events outside a limit angle Θ_{max} that typically amounts to about 45°. A natural proposition would be restricting the calculation to exactly this angular range. However, since the positions at the surface with launching angle $\Theta = \Theta_{max}$ are initially unknown, we cannot set proper boundary conditions here. We therefore decided to extend the calculation region to the circumference of the tip shaft (assumed cylindrical), since there the radius R_0 and the angle $\Theta_0 = 90°$ (see Fig. 3c) are *a priori* known. Due to symmetry, $R_I := R_0$ necessarily represents one of the main curvature radii. The other one is determined with the help of the Gaussian curvature ($R_{II} = (R_0 \cdot K)^{-1}$).

The missing information on the Gaussian curvature outside the angular range of the detector must be complemented by suitable assumptions on the general shape of an atom probe tip. A suggested solution is the postulation that the curvature outside equals the average curvature inside the detector range:

$$K(\Theta > \Theta_{max}) = \frac{\int_0^{\Theta_{max}} K \mathrm{d}\Omega}{\int_0^{\Theta_{max}} \mathrm{d}\Omega}. \tag{20}$$

As an alternative, one may also extrapolate the curvature field inside the detector to the outside (see the numerical examples below). For any choice, we have to make sure that the projection of the full surface area matches the cross-sectional area of the cylindrical shaft. This leads to the normalization condition

$$\int_0^{2\pi} \int_0^{\frac{\pi}{2}} \frac{\cos\Theta \sin\Theta \, \mathrm{d}\Theta \mathrm{d}\Phi}{K(\Theta, \Phi)} = \pi {R_0}^2, \tag{21}$$

which has to be fulfilled by multiplying the final curvature field by an appropriate constant.

Example calculations

In order to check the concept with field emitters of known surface shape, we numerically simulated the field evaporation of two sample tips with asymmetric evaporation properties, as presented in Fig. 4a and b. For both, an amorphous structure of about 10^6 atoms was generated by random sphere filling of a cylindrical shaft of 30 nm radius. We prefer a random amorphous structure to avoid complications by crystalline faceting. Subsequently, different evaporation thresholds were assigned to the atoms. For the first case shown in Fig. 4a, a stack of six layers with increasing steps of evaporation thresholds (from left to right: 51, 54, 57, 60, 63, 66 V nm^{-1}) was vertically oriented (*i.e.* tip axis parallel to the interfaces). For the second example in Fig. 4b, a 25% elevated threshold was assigned to the atoms within an off-axis spherical precipitate of 12 nm radius. Subsequently, the field desorption and the measurement of the events were simulated by the TAPsim† package,[26,27] which is particularly capable of handling random structures. The images in Fig. 4 represent the atomic structure after the evaporation of 300 000 atoms, when a stable steady state of the surface had developed. The significant deviation

† https://www.imw.uni-stuttgart.de/mp/forschung/atom_probe_RD_center/software/.

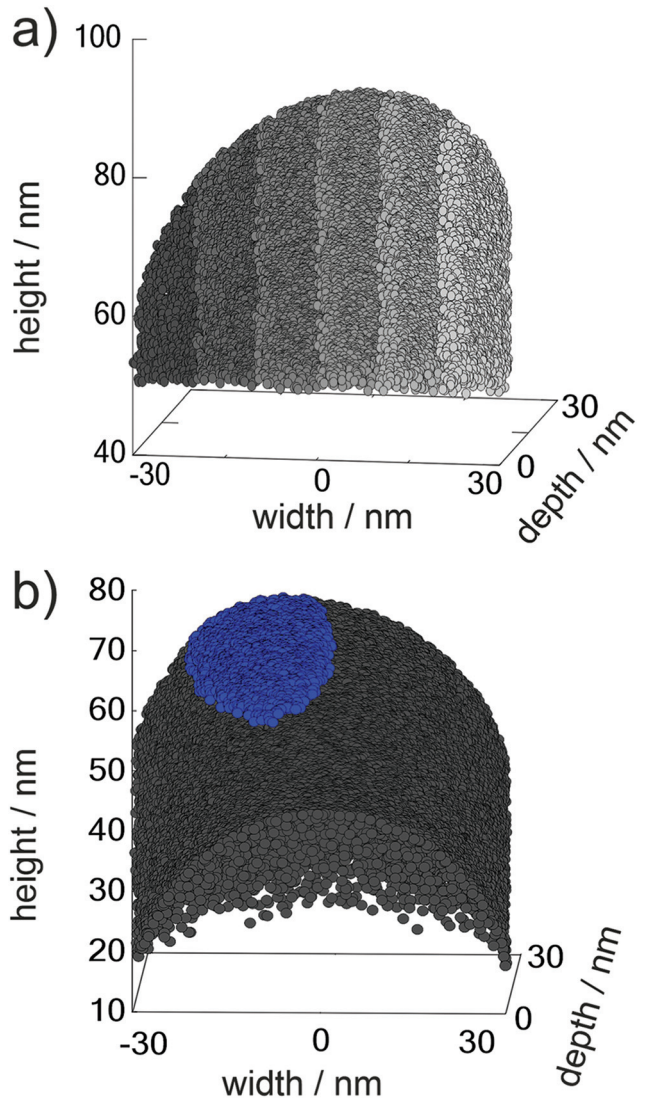

Fig. 4 Atomic structure of two test samples (for better understanding the tips are cut in half, view on the central mirror plane). Different colors or grey scales mark different evaporation thresholds. The steady states shown were obtained after evaporation of 300 000 atoms: (a) sample I, consisting of six layers with increasing evaporation threshold (from left to right, indicated by increasing brightness). (b) Sample II, containing an off-axis precipitate of elevated evaporation threshold marked in blue color. In both cases, the radius of the cylindrical shaft amounts to 30 nm, the radius of the precipitate is 12 nm.

from a hemisphere apex and the asymmetry with respect to the tip axis are obvious. In both structures, the curvature of the surface has increased locally where the evaporation threshold is high, to counterbalance reluctant evaporation by a stronger field. The tip shape of Fig. 4a closely resembles the reported shape of semiconductor tips with low heat conductivity after asymmetric laser irradiation,[28,29] and thus, represents a typical situation of a practical measurement. Also, the second geometry (Fig. 4b) is exemplary for common APT work, except for the fact that precipitates are usually significantly smaller than the tip diameter, since APT is preferentially used for ultimate microscopy. Due to the locally increased curvature, the precipitate protrudes from the surface, which would produce artificially diluted zones in the conventional volume reconstruction relying on a hemispherical apex.

Fig. 5 illustrates the calculation steps and result of the shape reconstruction for the first example, the tip with layers of stepwise increased evaporation threshold. Starting from the structure shown in Fig. 4a, the next 200 000 atoms were evaluated according to eqn (14) to determine the local event density. For a hemispherical apex, this density is expected to reveal a maximum at the tip axis. In contrast, the event density here appears left-weighted. The higher density is found on the side of lower curvature. (Additional ripples in the density reflect the original layered structure of the model.) Next, the local curvature is calculated from the discrete density by means of eqn (17), as shown in Fig. 5b by the blue circled data points. These can only be calculated within the angular range of the detector. However, since this curvature field varies almost linearly from left to right along the x-axis, we continue this slope to radially extrapolate into the angular range outside the detector (black crosses in Fig. 5b). Based on the so-calculated curvature field, the iteration of the finite difference method is performed. For the shown model calculation, we used a grid of 18 (radial) times 32 (azimuthal) points. For the initial configuration, the height profile has been set to the values of an ideal hemisphere of 30 nm radius. The next height approximations are calculated at all inner points from the heights of the respective eight neighbors and the curvature linked to the momentary surface normal at the given point. Only the points at the tip center and at the outer boundary need special treatments. The height in the center is calculated assuming a spherical cap of the appropriate curvature, the heights at the outer boundary are determined so that the discretized version of the boundary condition as illustrated in Fig. 3c is fulfilled.

Applied iteratively, this process converges to a stable end shape. The iteration loop was halted when the further modification of the height profile was less than 0.001 nm. In Fig. 5c, the profile of this end shape is shown at the mirror symmetry plane of the structure (yellow spheres), in comparison with the initial structure. The final residual between original and evaluated surface is plotted at the bottom of the figure. The deviation of the height profile is typically less than 2 nm, especially when considering the inner area seen by the detector. Given the fact that the extrapolation of the curvature to the outside angular range can only be an approximation, the agreement between both is well satisfactory.

The analogous procedure was applied to the second structure, of which the main steps of calculation are presented in Fig. 6. Here, the alternative proposition, setting the outer curvature constantly to the average of the inner measured points (black crosses and blue circles in Fig. 6b) appears more appropriate, since a precipitate provokes only a local disturbance of the surface. In this case the horizontal profile, shown by yellow circles in Fig. 6c, matches the mesoscopic shape quite well, but in detail some deviations at the precipitate still remain.

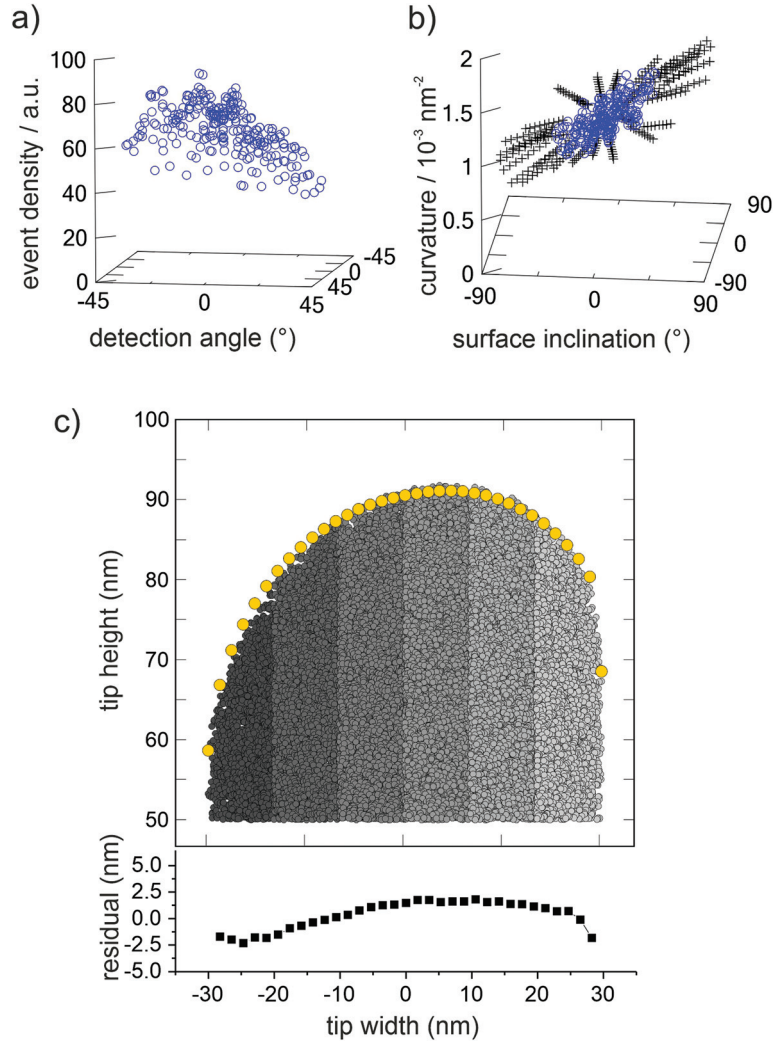

Fig. 5 Evaluation of the surface shape of test structure I: (a) local event density on the detector. In total, 200 000 atoms were considered to determine the density. The aperture of the detector was limited to 45°. (b) Gauss curvature as a function of the local surface orientation (inclination with respect to the tip axis and *x*-axis perpendicular to the layer stacking). Values derived from the measured densities (within an angle of 45°) are shown by blue circles, those obtained by extrapolation by black crosses. (c) Comparison between original tip structure and the surface profile at the mirror plane (yellow circles) as calculated by the proposed method. The residual between the real surface profile at the tip symmetry plane and the evaluated profile is plotted at the bottom.

It appears that these remaining deviations stem from a slightly concave surface at the boundary between matrix and precipitate. The concave part at the boundary lets the precipitate protrude slightly more than predicted by the mathematical model. In addition, the extrapolation model may contribute to this deviation. If the extrapolation to the outer angular range overestimates the curvature, the curvature at the precipitate becomes erroneously reduced as a consequence of the normalization according to eqn (21).

Evaluation of experimental data

The accuracy achieved in the previously shown examples leaves room for improvement by choosing finer grid spacing and better suited extrapolation models. Nevertheless, an experimental example should demonstrate that the proposed method is already sufficient to obtain a decisive improvement in the reconstructions. It shall also demonstrate that additional experimental factors that may affect the event density on the detector, such as redistribution at zone lines and poles or the uncontrolled loss of atoms between pulses do not compromise the proposed method. Since dealing with the transition stages between different steady-state emitter profiles needs further considerations, we chose an experimental situation in which the formation of a steady surface is warranted: a multilayer in vertical alignment (tip axis parallel to the interfaces) which is an experimental situation prone to magnification artefacts. For this demonstration, Cr/(Al-oxide/Al)$_n$/Cr multilayers were prepared by depositing chromium and aluminum layers by physical evaporation and oxidizing the surface of the aluminum layers in an RF-generated oxygen plasma

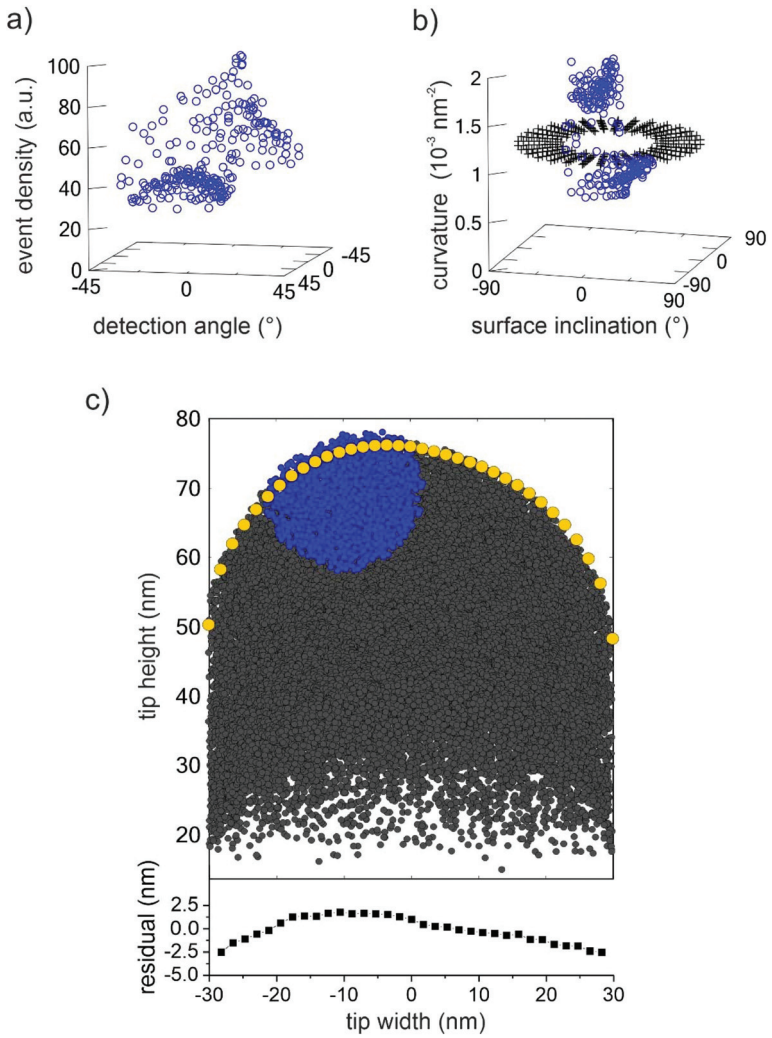

Fig. 6 Evaluation of the shape of test structure II: (a) local event density on the detector. In total 200 000 atoms were considered to determine this density. The aperture of the detector was limited to 45°. (b) Gauss curvature as a function of the local surface orientation. Values derived from the detector densities (within an angle of 45°) are represented by blue circles, those obtained by extrapolation are indicated by black crosses. (c) Comparison between original tip structure and the surface profile along the *x*-axis (yellow circles) as evaluated from the detector data. The residual between the real surface profile at the tip symmetry plane and the evaluated profile is plotted at the bottom *versus* a radial coordinate.

(oxygen flow rate: 30 sccm; oxygen partial pressure: 10 mTorr; RF power: 200 W; duration: 30 s) to form the aluminum oxide. The layer thicknesses are well controlled and documented by TEM in cross section geometry, as demonstrated in Fig. 7a. Especially, the Al-oxide layers reveal a homogeneous thickness of (6 ± 0.5) nm. A piece of the same lamella, containing an Al oxide layer embedded between Cr and Al, was mounted on a tungsten post in vertical alignment and thinned by azimuthal milling to a suitable end shape. Laser-assisted APT analysis was performed over several million atoms to develop a steady state shape of the tip surface.

Of these data, a block with 1.3×10^6 events was selected. Since the mass spectra contain various species (O, Al, Cr, AlO, Al_2O and Al_2O_2) significantly different in size, the realistic partial volumes were considered (0.0232, 0.0166, 0.0120, 0.0398, 0.0564 and 0.0796 nm^3, respectively).

In calculation of the tip shape, we chose a further variant of the required curvature extrapolation into the non-measured region: for each azimuth Φ, K is linearly interpolated between the outermost measured curvature towards $K = R_0^{-2}$ at the shaft. The resulting tip surface is shown in Fig. 7b.

Obviously, the curvature of the tip became elevated at the Al-oxide layer. The asymmetric deviation from the spherical shape leads to strong shifts of the events on the detector that are, however, neglected in the Bas *et al.* scheme. These shifts can be best documented by a mesh following the iso-r and iso-φ contours of the tip coordinates overlaid on the color-coded events on the detector plane (Fig. 7c). The vertices of this mesh are calculated by projection from the grid points of the height profile along the local surface normal. Even though the tip shaft is cylindrical, this mesh and, therefore, the measured part of the tip cross section are not circular symmetric

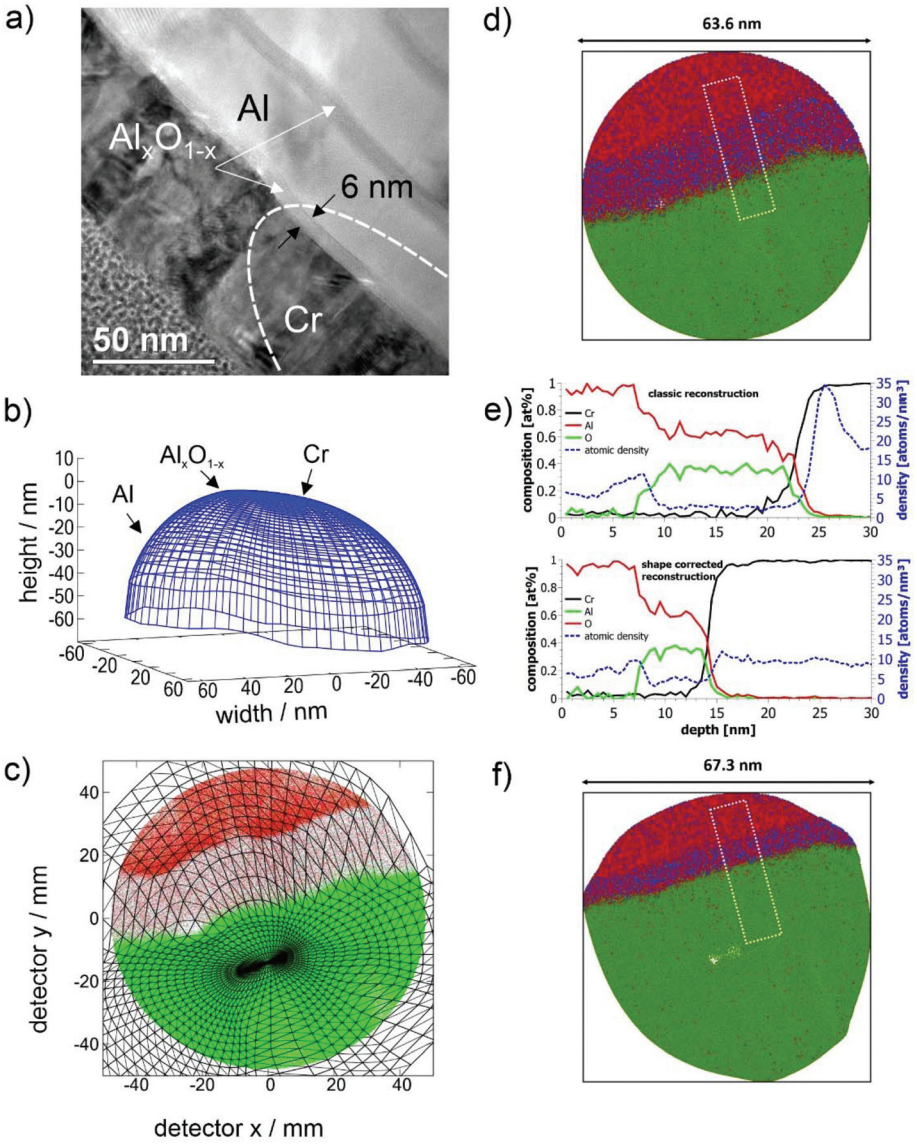

Fig. 7 Reconstruction of experimental data of a Cr/Al-oxide/Al tri-layer: (a) cross section TEM micrograph (a region equivalent to the investigated atom probe tip is indicated in white dashes). (b) Tip profile as derived from the event distribution. (c) Assignment of lateral tip coordinates to the detector positions. Measured events are presented as color-coded dots (Al red, Cr green, O light blue). The real-space tip coordinates are shown by a mesh of iso-r and iso-ϕ contours (thick lines). (d) Reconstruction with the classical Bas *et al.* protocol (viewing direction along the tip axis). Position and direction of concentration profiling are indicated by a dashed rectangle. (e) Composition and density profiles determined perpendicular to the interfaces for the classical (top) and the shape-corrected scheme (bottom). (f) Reconstruction obtained by the new shape-corrected method.

anymore. Larger facets on the oxide layer demonstrate that oxygen containing events stem from a relatively smaller surface fraction of the tip.

Now we perform the volume reconstructions. The result of the classical reconstruction (in wide angle modification) is shown in Fig. 7d. Clearly, the Al-oxide layer appears strongly oversized in thickness and in compensation, its atomic density is far too low. This can best be seen in the composition and density profiles (shown in Fig. 7e, top) determined in stacking direction. In the density profile (blue dashed), we observe peaks of strongly increased density at the interfaces just outside the oxide. In this way, local magnification effects become very obvious. They are due to the contrasting evaporation thresholds in the order $E_{Al} < E_{Cr} < E_{Al_xO_{1-x}}$.

In the proposed shape-corrected reconstruction, we shift the atoms to their correct position with the help of the distortion map of Fig. 7c. This computation step is performed most efficiently by triangulation of the mesh and linear interpolation of the atom positions between the already determined vertices. The so calculated reconstruction is shown in Fig. 7f (view along the tip axis). Remarkably the measured volume is by far not cylindrical any more. Instead, the border line indicates the different evaporation thresholds, *i.e.* the curvature of the border is more pronounced at the Al-oxide compared to

the neighbor layers. The volume fraction of Cr has been significantly elevated with respect to Al and Al-oxide. The corresponding profiles through the oxide layer are shown in Fig. 7e (bottom), in direct comparison to those of the classical protocol. As a remarkable success, the Al-oxide now appears in its correct thickness very close to 6 nm without any further calibration (both reconstructions used the same partial volumes for the detected molecules). Also the number density (see Fig. 7e, dashed) becomes practically homogeneous within each layer and the different density levels match reasonably to the relation between the average atomic volumes ($\Omega_{\text{Al-oxide}} > \Omega_{\text{Al}} > \Omega_{\text{Cr}}$).

Discussion

In a recent report[22] on axial symmetric samples, we already demonstrated that a shape extraction, based on the statistical interpretation of the event density, can improve the quality of APT volume reconstructions decisively. This statement is now fully corroborated by the generalization to non-axial symmetric geometries and the experimental example shown in the previous section. Since the proposed algorithm for non-axial symmetric samples reproduces the surface shapes of critical model structures quite well, we do expect that a decisive improvement of the reconstruction can be obtained in many experimental situations.

The main advantage of the proposed method is that it corrects the density fluctuations by redistribution *i.e.* correctional shifts of the atoms. A shift of the atoms to homogenize the density has been previously proposed, but only as an *a posteriori* processing step after the first reconstruction had been achieved. This typically leaves arbitrariness of how to distribute the necessary compression or expansion to the three dimensions of space. The here proposed method of determining the atom positions from the realistic shape of the tip surface during evaporation clarifies this issue unambiguously, based on a proper consideration of the measurement process.

Noteworthy, the proposed statistical interpretation is practically not affected by the finite detector efficiency. Nevertheless, a high quality of measurement is required that avoids uncontrolled loss of events and still, poles or zone lines should be avoided or the resolution of the density evaluation must be sufficiently coarse that the respective redistribution of the events is averaged out.

With the three presented alternatives for the extrapolation of the curvature into the non-measured part of the tip, which all lead to a reasonable description of the tip geometry, we have shown that the required extrapolation is feasible. However, it introduces at least a certain arbitrariness into the evaluation. The investigation of further model structures may lead to refined extrapolation models of the curvature and, consequently, to a more accurate description than presented in Fig. 5c and 6c.

To our present knowledge, we cannot show mathematical proof that the described numerical procedure always has an unambiguous convex solution. Since the curvature is not directly known at given positions, but only indirectly *via* their respective surface inclinations that change during the iteration, the situation is mathematically less transparent. We cannot exclude that for some pathologic distribution of events, multiple solutions would satisfy all equations. For the model cases studied, we checked that different starting conditions (*e.g.* starting from a hemisphere or a circular disk) lead to the same result. We indeed found that, the end shape was independent of the choice of the starting conditions. Therefore, we presume that a unique end shape will be discovered for any physically reasonable distribution of events.

Other mathematically technical issues concern the stability and convergence of the iteration scheme. Not in the shown examples, but in some other tested tip geometries, it was required to superpose the height profiles of the l^{th} and the $(l + 1)^{\text{th}}$ iteration to assure convergence. To illustrate the typical convergence behavior, Fig. 8 shows a plot of the maximum variation of the height profile between two iteration steps *versus* the number of steps for the model calculation shown in Fig. 5. Within about 3000 iterations the variation approaches a minimum residual value. This residual depends on the chosen discretization and boundary conditions. Thus, it can be used as a measure for the quality of approximation. In our experience, its value can be obtained smaller than ±0.001 nm. Presumably, it would also be possible to construct higher order schemes that rely on a larger number of neighbor grid points to stabilize the convergence and to achieve even more accurate solutions.

When it comes to the realization of practical reconstruction protocols, numerical effort is a critical issue. Since the proposed shape extraction is based on the evaluation of a large number of atoms, it is neither required nor recommended to recalculate the shape in each reconstruction step for a single atom. Instead, in the practical situation with data sets of 10^8 events, it seems reasonable to apply the shape extraction to subsets of 100 000 to 500 000 atoms. (At least a few monolayers

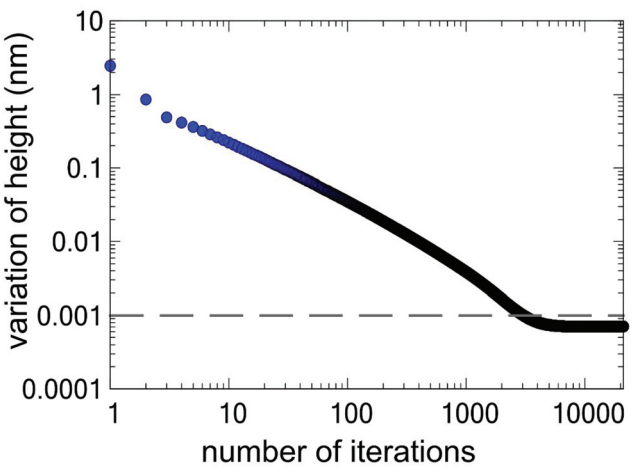

Fig. 8 Convergence behaviour of the iterations in the finite difference procedure: maximum variation of the height profile between two iterations *versus* the number of the iteration loop.

at the surface must be comprised to yield statistical reliability.) Thus, a recalculation of the shape would be required after reconstruction of about 10^5 atoms. Run on a business laptop computer without any parallel coding, a single shape extraction on 36 × 64 grid points needs about 10 s of calculation time. This duration scales with the number of grid points, but is practically independent of the number of atoms in the data set, since performing the finite difference iteration is critical, while the time for calculating the detector densities is negligible. In addition, the iteration loop is well suited for an effective parallelization, which could reduce the calculation time by an order of magnitude. So, we reasonably expect that the computing time for one shape extraction can be restricted to about 1s. In conclusion, performing the reconstruction of 10^8 events by calculating a new surface shape every 10^5 atoms would lead to about 1h total processing time, which is very acceptable for a careful final reconstruction of experimental data.

In order to become computationally effective, the presented algorithm avoids calculating ion trajectories. Instead, it uses the simple projection law expressed by eqn (2) together with the identification between the detection and launching azimuth. It must be mentioned that eqn (2) has been deduced from field ion microscopy of ideally shaped samples. In the case of an asymmetric or rough apex, it only represents an approximation of which we expect less accuracy the more the tip surface deviates from a sphere. To estimate the quality of this approximation, we investigated the considered model structures with trajectory calculations using the TAPSim[13] program. Fig. 9 compares the launching azimuth Φ with the detection azimuth Φ_D for about 200 000 events of (i) a well-developed homogeneous tip and of the already presented asymmetric geometries containing (ii) an off-axis precipitate or (iii) the layer stack of varying evaporation thresholds (from top to bottom, as labeled). For each case, the deviation between both angles is plotted *versus* the detection azimuth. Grey dots represent individual trajectories, the solid blue line the average at a given detection angle.

For the ideal hemispherical apex (top), the expected identity between both launching and detection azimuth is clearly confirmed for the average. Still, the scatter among individual trajectories (grey dots) is remarkable. Its standard deviation ranges from 5° to 7°. This scatter contributes to the well-known limitation of APT resolution in the lateral directions. Indeed, for the two asymmetric tip geometries (middle and bottom), an additional systematic deviation between both azimuth angles is seen. This deviation reveals a mirror symmetry around 0° and 180°, as expected for a surface geometry with a central mirror plane, but in both cases, its magnitude remains less than 3°. The deviations of the polar angle from eqn (2) are of similar magnitude.

Whether such deviations are small or large, must be decided in comparison to other relevant disturbances. First, the natural scatter of the individual trajectories is obviously more than twice as large, and second, the calculation of the event density on the detector has been done with an azimuthal discretization even larger than 10°. In view of this comparison,

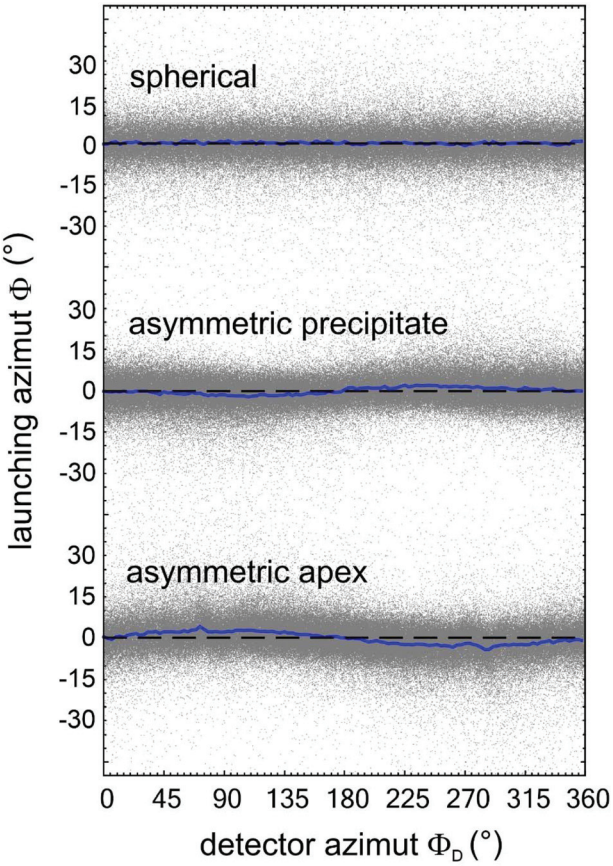

Fig. 9 Evaluation of trajectories in terms of the launching and detection azimuth for the three exemplary apex geometries: hemispherical, asymmetric precipitate and asymmetric layer stack (from top to bottom as labelled). The deviation between both angles is plot *versus* the azimuth on the detector. Grey dots represent results of individual trajectories, solid (blue) the average at given Φ_D.

we conclude that the deviation from the projection law is probably negligible in the shown cases, but it can become significant, if a higher spatial resolution is desired. In this case, sooner or later, one reaches the point that trajectory calculations become unavoidable. It might be sufficient to calculate them only for the small set of discrete points of the height profile. Since their number is relatively small, this step could possibly already be integrated into the iteration loops when solving the differential equation eqn (13). However, we need to postpone a presentation of respective results and the discussion of this generalization to a later communication.

Conclusions

In this work, we presented a mathematical model to extract the surface of atom probe tomography samples from the event distribution on the entrance aperture of the detector.

• The model is applicable to sample surfaces of arbitrary shape. Only a differentiable convex shape of the surface has to be postulated.

• It is shown, in general, that the event density on the detector correlates inversely to the Gaussian curvature, if the atomic structure roughness at the surface is neglected. A finite difference method is derived to determine the real space surface shape iteratively from the curvature field.

• The convergence of the method to a unique solution and the accuracy of this solution have been demonstrated by calculating two model structures, an asymmetrically field-evaporated tip and a protruding off-axis precipitate.

• The method has also been demonstrated by successfully reconstructing concrete experimental data. The computational effort of the method allows designing a full reconstruction protocol for experimental data sets of hundreds of millions of atoms in reasonable computing time.

Conflicts of interest

There are no conflicts to declare.

Acknowledgements

Financial support by the Deutsche Forschungs-Gemeinschaft (DFG grant SCHM 1182/16-2 as well as collaborative research center CRC 1333/C3) is gratefully acknowledged. The used dual beam microscope was jointly funded by the Baden-Württemberg-Stiftung and the Deutsche Forschungs-Gemeinschaft (INST41/982-1 FUGG). Individual contributions of the authors: D. B.: computer programming, design of numerical model structures, testing of various concepts, introduction of triangulation, TAPSim simulations; F. B.: basic equations of differential geometry, mathematical design of the finite differences loop; H. S.: FIB preparation, APT analysis, data evaluation of the multilayer sample; R. A. & H. K.: deposition of the multilayer system; G. S.: development of the principal concepts of shape extraction, Gaussian curvature and its extrapolation, design of the numerical algorithms, writing of the manuscript.

References

1 M. K. Miller and R. G. Forbes, *Atom probe tomography, The Local Electrode Atom Probe*, Springer, London, 2014.
2 D. J. Larson, T. J. Prosa, R. M. Ulfig, B. P. Geiser and T. F. Kelly, *Local electrode Atom Probe Tomography, A User's Guide*, Springer, London, 2013.
3 B. Gault, M. P. Moody, J. M. Cairney and S. P. Ringer, *Atom Probe Microscopy, Springer series in Materials Science*, Springer, London, 2012.
4 D. Beinke, C. Oberdorfer and G. Schmitz, Towards an accurate volume reconstruction in atom probe tomography, *Ultramicroscopy*, 2016, **165**, 34–41.
5 P. Bas, A. Bostel, B. Deconihout and D. Blavette, A general protocol for the reconstruction of 3D atom probe data, *Appl. Surf. Sci.*, 1995, **87/88**, 298–304.
6 F. Vurpillot, A. Bostel and D. Blavette, The shape of field emitters and the ion trajectories in three-dimensional atom probes, *J. Microsc.*, 1999, **196**, 332–336.
7 E. A. Marquis, B. P. Geiser, T. J. Prosa and D. J. Larson, Evolution of tip shape during field evaporation of complex multilayer structures, *J. Microsc.*, 2010, **241**, 225–233.
8 C. Oberdorfer and G. Schmitz, On the Field Evaporation Behaviour of Dielectric Materials in Three-Dimensional Atom Probe: A Numeric Simulation, *Microsc. Microanal.*, 2011, **17**, 15–25.
9 S. Gerstl, B. Geiser, T. Kelly and D. Larson, Evolution of local radii of atom-probe-tomography specimens, *Microsc. Microanal.*, 2009, **15**, 248–249.
10 F. Vurpillot, A. Cerezo, D. Blavette and D. J. Larson, Modeling Image Distorsions in 3DAP, *Microsc. Microanal.*, 2004, **10**, 384–390.
11 F. Vurpillot, A. Bostel and D. Blavette, Trajectory overlaps and local magnification in three- dimensional atom probe, *Appl. Phys. Lett.*, 2000, **76**, 3127–3129.
12 M. K. Miller and M. G. Hetherington, Local magnification effects in the atom probe, *Surf. Sci.*, 1991, **246**, 442–449.
13 D. J. Larson, B. Gault, B. P. Geiser, F. De Geuser and F. Vurpillot, Atom probe tomography spatial reconstruction: Status and directions, *Curr. Opin. Solid State Mater. Sci.*, 2013, **17**, 236–247.
14 B. Gault, D. Haley, F. de Geuser, M. P. Moody, E. A. Marquis, D. J. Larson and B. P. Geiser, Advances in the reconstruction of atom probe tomography data, *Ultramicroscopy*, 2011, **111**, 448–457.
15 B. Gault, S. T. Loi, V. J. Araullo-Peters, L. T. Stephenson, M. P. Moody, S. L. Shrestha, R. K. W. Marceau, L. Yao, J. M. Cairney and S. P. Ringer, Dynamic reconstruction for atom probe tomography, *Ultramicroscopy*, 2011, **111**, 1619–1624.
16 B. P. Geiser, D. J. Larson, E. Oltman, S. Gerstl, D. Reinhard and T. F. Kelly, Wide-Field-of-View atom probe reconstruction, *Microsc. Microanal.*, 2009, **15**(Supplement S2), 292–293.
17 S. K. Suram and K. Rajan, Calibration of reconstruction parameters in atom probe tomography using a single crystallographic orientation, *Ultramicroscopy*, 2013, **132**, 136–142.
18 F. De Geuser, W. Lefebvre, F. Danoix, F. Vurpillot, B. Forbord and D. Blavette, An improved reconstruction procedure for the correction of local magnification effects in three-dimensional atom-probe, *Surf. Interface Anal.*, 2007, **39**, 268–272.
19 N. Rolland, D. J. Larson, B. P. Geiser, S. Duguay, F. Vurpillot and D. Blavette, An analytical model accounting for tip shape evolution during atom probe analysis of heterogeneous materials, *Ultramicroscopy*, 2015, **159**, 195–201.
20 N. Rolland, F. Vurpillot, S. Duguay and D. Blavette, Dynamic evolution and fracture of multilayer field emitters in atom probe tomography: a new interpretation, *Eur. Phys. J.: Appl. Phys.*, 2015, **72**, 21001.

21 N. Rolland, F. Vurpillot, S. Duguay, B. Mazumder, J. S. Speck and D. Blavette, New Atom Probe Tomography Reconstruction Algorithm for Multilayered Samples: Beyond the Hemispherical Constraint, *Microsc. Microanal.*, 2017, **23**, 247–254.
22 D. Beinke and G. Schmitz, Atom probe reconstruction with a locally varying emitter shape, *Microsc. Microanal.*, 2019, **25**, 280–287.
23 A. Cerezo, P. Warren and G. Smith, Some aspects of image projection in the field-ion microscope, *Ultramicroscopy*, 1999, **79**, 251–257.
24 A. Pressley, *Elementary Differential Geometry (Thm 8.1.6)*, Springer, Berlin, 2012.
25 A. Gray, *Modern Differential Geometry of Curves and Surfaces with Mathematica*, CRC Press, Boca Raton, 2nd edn, 2006.
26 C. Oberdorfer, S. M. Eich and G. Schmitz, A full-scale simulation approach for atom probe tomography, *Ultramicroscopy*, 2013, **128**, 55–67.
27 C. Oberdorfer, S. M. Eich, M. Lütkemeyer and G. Schmitz, Applications of a versatile modelling approach to 3d atom probe simulations, *Ultramicroscopy*, 2015, **159**, 184–194.
28 S. Koelling, N. Innocenti, A. Schulze, M. Gilbert, A. Kambham and W. Vandervorst, In-situ observation of non-hemispherical tip shape formation during laser-assisted atom probe tomography, *J. Appl. Phys.*, 2011, **109**, 104909.
29 A. Shariq, S. Mutas, K. Wedderhoff, C. Klein, H. Hortenbach, S. Teichert, P. Kücher and S. S. A. Gerstl, Investigations of field-evaporated end forms in voltage- and laser-pulsed atom probe tomography, *Ultramicroscopy*, 2009, **109**, 472–479.

